Laboratory Characterization of Silicon Avalanche Photodiodes (APDs) for Pulse-Position Modulation (PPM) Detection

M. Srinivasan,[1] J. Hamkins,[1] B. Madden-Woods,[1] A. Biswas,[1] and J. Beebe[1]

Two commercially available large-area silicon avalanche photodiodes (APDs) were characterized in the laboratory. The response of the APDs to a sequence of 8-bit pulse-position modulated (256-PPM) laser pulses, with and without additive background noise, was recorded and stored for post-analysis. Empirical probability density functions (pdf's) were constructed from the signal and noise slot data and compared to pdf's predicted by an analytical model based on the sum of Webb and Gaussian (Webb+Gaussian) statistics. The pulse sequence was used to generate bit-error rate (BER) versus signal photons-per-pulse plots. These BER measurements were also compared with analytical results obtained by using the Gaussian and Webb+Gaussian models for APD channel statistics. While the 532-nm APD data showed reasonable coherence with theory, more discrepancies were evident in the 1064-nm APD case. It is surmised that these discrepancies were caused by inaccurate knowledge of detector parameters as well as radio frequency interference. A simple slot synchronization loop was also tested on the laboratory-generated detector output data, resulting in little to no loss upon use of the tracking-loop-generated timing in calculation of bit-error probabilities.

I. Introduction

A progress report on laboratory characterization of silicon avalanche photodiodes (APDs) is presented. The effort is motivated by the need to develop pulse-position modulated (PPM) receivers [1] required for deep-space optical communications. The APD is a likely candidate for the front-end opto-electronic conversion device required by the receivers. Previous studies [2] have established that high-peak-power laser transmitters are necessary for viable optical links required for future NASA interplanetary missions. Consequently, PPM laser transmitters have been identified as candidates for providing deep-space communications needs. Popular wavelengths at which the required peak power can be achieved are the fundamental and second harmonics of Nd:YAG, Nd:YVO4, and Nd:YLF lasers. As a result, 532 nm and 1064 nm were chosen for detector characterization. From a system engineering point of view, the 1064-nm wavelength is preferable, as a 3-dB power penalty is incurred with use of the frequency-doubled 532 nm. In addition, greater vulnerability to atmospheric turbulence and background noise exists at

[1] Communications Systems and Research Section.

The research described in this publication was carried out by the Jet Propulsion Laboratory, California Institute of Technology, under a contract with the National Aeronautics and Space Administration.

532 nm. However, significantly improved detector quantum efficiency (by a factor of two) can be realized at 532 nm as compared with 1064 nm.

The PPM receivers are being developed to operate in conjunction with large-aperture (10-m-diameter) ground-based non-imaging-quality telescopes. Therefore, the laser signal must traverse an atmospheric path prior to collection and focusing by the telescope. Previous analysis [3] has shown that atmospheric turbulence will limit the achievable focal spot sizes even with a perfect surface-quality 10-m F2 telescope to approximately 2 mm in diameter. Furthermore, the non-imaging ("photon bucket") telescopes being considered in order to reduce cost of implementation will only add to the focal spot sizes. With this in mind, commercially available 3-mm-diameter detectors for 532-nm and 1064-nm wavelengths were chosen for characterization. Large single-detector areas typically introduce bandwidth limitations as a consequence of increased capacitance. Reduced bandwidth can restrict the detector's ability to resolve the received laser pulses, thereby necessitating an increase in the PPM slot width. However, increasing the slot width increases the vulnerability to background noise. Furthermore, not being able to resolve the laser pulse compromises the ranging ability of a deep-space optical communications receiver, a function that is highly desirable.

Photon-counting detectors can provide shot-noise-limited performance. However, the performance of commercially available state-of-the-art photon-counting devices has not been completely quantified in the laboratory in the presence of background noise. The objective of the present study is to evaluate thermal-noise-limited detectors in the presence of background noise. Given this limitation, the highest achievable quantum efficiency and lowest noise characteristics were sought.

Previous reports on APD detector characterization have usually used a 4-PPM modulation scheme [4]. Moreover, current modulated diodes (810–860 nm) [4] and intensity-modulated solid-state lasers (1064 nm) [5] were used to achieve the APD characterization. Sensitivities of 264 incident photons/bit for a bit-error rate of 10^{-6} were reported at 1064 nm using such a scheme. In the present work, a Q-switched solid-state laser modulated using 256-PPM with 50–100 kHz repetition rates (compared to the Mb/s used previously) was used. The objective of the work was to compare laboratory measurements with the analytical models described in [4,6] as well as to test the absolute performance of detection and slot synchronization algorithms on real detector data.

II. Experimental Setup

An Advanced Photonix Model 118-70-74-641 thermoelectrically cooled APD module and a near-infrared enhanced Perkin Elmer (formerly EG&G) 30659G APD integrated to a custom high-voltage temperature-controlled (HVTC) board were used at 532 and 1064 nm. In Fig. 1 we show a schematic representation of the experimental arrangement used. A Q-switched Nd:YVO_4 laser oscillator [7] was used to provide 1064-nm light with a pulse width that varies from 1–3 ns for repetition rates of 1–100 kHz. When 532-nm light was being used for detector characterization, the 1064-nm light was transmitted through a focusing lens and a lithium niobate crystal frequency-doubler assembly shown in Fig. 1. The collimated laser beam at 1064 or 532 nm was incident through a variable attenuator and pellicle beam splitter on a lens that focused the light to a small spot. The light path following the lens was split by a second pellicle beam splitter so that it was simultaneously incident upon a power sensor (Anritsu Model MA9802A) and the APD to be characterized. The splitting ratio of the 532- and 1064-nm light was calibrated separately by moving the power sensor back and forth between the two locations.

The pellicle beam splitter preceding the lens in the light path allowed the introduction of additive background noise from a tungsten source emitted through a light pipe. The white light was filtered using a narrowband pass filter (10 nm at 532 nm and 3 nm at 1064 nm).

The laser was externally modulated using the PPM modulator, which consists of an electronic timing circuit that can simulate a restricted version of 256-PPM in which the pulses are stepped sequentially

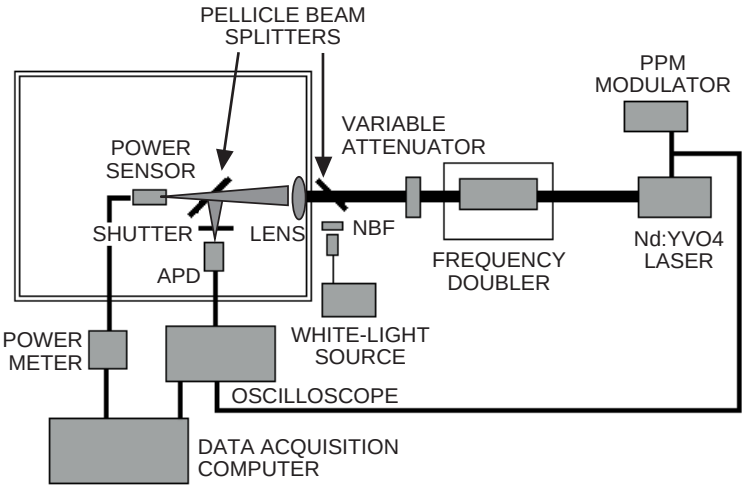

Fig. 1. A schematic layout of the experimental arrangement used for performing the detector characterization.

through the 256 slots using a ring counter. The slot width can be independently varied at the chosen pulse rate. In the results to be presented, 50-kHz (532 nm) and 100-kHz (1064 nm) repetition rates with 25-ns slot widths were used.

The power sensor, APD, and lens assembly were enclosed inside a light-tight box with a hole to admit the laser and white light. An electronic shutter operated remotely from outside the enclosure (not shown in the figure) allowed blocking of the APD.

The procedure followed for acquisition of PPM data consisted of attenuating the laser beam to low pulse powers so that only a few signal pulses would be observed by the sampling oscilloscope in order to define the measurement range for this experiment. A data stream was recorded for post-analysis. The attenuation was gradually reduced while pulse sequences were recorded. The low average powers used were usually below the −65-dBm sensitivity level of the power sensor; however, by using the remotely operated electronic shutter, the detector could be blocked and the power recorded without attenuation. This power could then be converted to average power incident on the detector using known attenuation values calibrated separately. This was found to be the most reliable method of determining the average incident power, from which the average numbers of photons per pulse were determined.

A Tektronix 754C oscilloscope was used to record the pulse streams. This oscilloscope has an extended acquisition mode that allows the recording of 8 million records. Half of this available storage capacity was used to record synchronous PPM trigger on one of the channels while the remaining half was used to store the APD output. With sampling and pulse repetition rates of 500 Msamples/s and 50 kHz, respectively, for the 532-nm APD, and 1 Gsample/s and 100 kHz for the 1064-nm APD, a total of 400 signal pulses was recorded for each data run. Matlab and C routines have been developed for detecting the number of pulses received using a maximum-likelihood algorithm [6]. The output of the maximum-likelihood algorithm can be compared with the recorded trigger pulses where the laser is known to have fired in order to obtain symbol- and bit-error rates.

III. Comparison of Results with Theory

Laboratory performance is evaluated through comparisons of the measured APD output statistics and PPM bit-error probabilities with analytical probability density functions and error-rate calculations. If the distributions of the APD output statistics for signal and noise (non-signal) slots in the empirical data match the theoretical probability density functions well, more confidence may be placed in basing

system designs upon the theoretical models. We provide a number of plots that compare the empirically constructed densities of signal and non-signal slots to those predicted by theoretical analysis and approximation, and we compare the experimental and theoretical bit-error rates for a detection algorithm under the assumption of perfect time synchronization.

A. Analytical Model of the APD Channel

Following the formulation found in [4], we model the output of the APD photodetector package as the sum of Webb and Gaussian (Webb+Gaussian) random variables. The average number of photons absorbed by an APD illuminated with total optical intensity $\lambda(t)$ in T_s seconds may be expressed as

$$\bar{n} = \frac{\eta}{h\nu} \int_0^{T_s} \lambda(t) dt \tag{1}$$

where h is Planck's constant, ν is the optical frequency, and η is the detector's quantum efficiency, defined as the ratio of absorbed to incident photons. The actual number of photons absorbed, n, is a Poisson-distributed random variable. The probability $p(m|\bar{n})$ that an APD generates m output electrons given $\bar{n}$ mean absorbed photons can be derived from the McIntyre–Conradi distribution [8], but may be approximated by the continuous Webb density function [9] as follows:

$$p(m|\bar{n}) = \frac{1}{\sqrt{2\pi\bar{n}G^2F}\left(1 + \dfrac{m - G\bar{n}}{\bar{n}GF/(F-1)}\right)^{3/2}} \exp\left(-\frac{(m - G\bar{n})^2}{2\bar{n}G^2F\left(1 + \dfrac{m - G\bar{n}}{\bar{n}GF/(F-1)}\right)}\right) \tag{2}$$

Here, G is the average APD gain, k is the ionization ratio, and F is the excess noise factor given by $F = kG + (2 - 1/G)(1 - k)$. Added to the random number of APD output electrons is an independent Gaussian thermal noise charge from the follow-on electronics [4]. The probability density function for the slot statistic is therefore the convolution of the Webb and Gaussian density functions, and may be written as

$$p(x|\bar{n}) = \sum_{m=0}^{\infty} \phi(x, \mu_m, \sigma^2) p(m|\bar{n}) \tag{3}$$

where $\phi(x, \mu_m, \sigma^2)$ is the Gaussian density function with mean $\mu_m = mq + I_sT_s$ and variance $\sigma^2 = (2qI_s + [4\kappa T/R])\, BT_s^2$, as given in [4]. Here, q is the electron charge, κ is Boltzmann's constant, T is the equivalent noise temperature, I_s is the APD surface leakage current, and B is the single-sided noise bandwidth. The value of the load resistance, R_L, is given by the feedback resistance of the transimpedance amplifier following the APD. Note that the APD surface leakage current is not multiplied by the APD gain and is modeled here as a constant DC current. The bulk dark current, I_b, on the other hand, is multiplied by the APD gain and is modeled as part of the background radiation.

An approach that is commonly used to simplify calculation of PPM symbol-error probabilities is to model the density of the APD output electron charge as Gaussian with mean $qG\bar{n}$ and variance $q^2G^2F\bar{n}$. Then the slot statistic consisting of the sum of APD output electrons and amplifier thermal noise is also Gaussian, and has mean $\mu = qG\bar{n} + I_sT_s$ and variance $\sigma^2 = \left[2q^2G^2F\bar{n} + qI_sT_s + (4\kappa TT_s/R_L)\right] BT_s$. Although simple, this approximation does not yield accurate results over all regions of interest, as previously shown in [4].

For M-ary PPM with slot duration T_s, the total charge is integrated over each slot time T_s, resulting in a vector of M independent observables for each received PPM word. It was shown in [6] that, given

these observables, the maximum-likelihood detector structure consists of choosing the PPM symbol corresponding to the slot with the largest accumulated charge value. If $\bar{n}_b$ and $\bar{n}_s$ are the mean number of absorbed background photons per slot and the mean number of absorbed signal photons per pulse, respectively, the M-ary PPM symbol-error probability is

$$P_e(M) = 1 - \int_{-\infty}^{\infty} p(x|\bar{n}_b + \bar{n}_s) \left[\int_{-\infty}^{x} p(y|\bar{n}_b) dy \right]^{M-1} dx \tag{4}$$

where $p(x|\bar{n})$ is given in Eq. (3).

B. Probability Density Function Comparisons

Output voltage signals from the 532-nm APD and 1064-nm APD were sampled at rates of 500 Msamples/s and 1 Gsample/s, respectively, and accumulated to form 25-ns slots (12.5 or 25 samples per slot). These slots were then separated into signal and non-signal (noise) slots. Note that these slot statistics are in units of accumulated voltage over a slot, whereas the analytical model of the previous subsection was presented in terms of accumulated slot charge. In the plots, the charge is simply converted to voltage across the load resistor by multiplying by qR_L/T_{sample}, where T_{sample} is the sample time.

The slot counts can be put into a histogram in order to obtain an empirical probability density function (pdf). Due to the high order of PPM signaling used and the amount of dead time between PPM words (50-kHz repetition rate for the 532-nm APD and 100-kHz repetition rate for the 1064-nm APD), there are significantly more noise slots than signal slots, i.e., there are 400 signal slots and over 300,000 noise slots in the collected data sets. This results in an empirically observed noise slot pdf that should be quite close to the actual pdf, while the empirical signal pdf is expected to exhibit more random variation.

The parameters required to predict the pdf's of the APD outputs are given in Table 1. These values are as reported or published by the APD vendors and most were not independently confirmed. The noise equivalent bandwidth is approximated to be $B = 1/(2T_s)$ Hz, which is that of an ideal integrator over duration T_s. The APD output distributions were found to be particularly sensitive to the values of the equivalent noise temperature and the average APD gain, so an attempt was made to measure these values. For the 532-nm APD, the equivalent noise temperature was estimated by tuning the gain to nearly zero

Table 1. System parameters for the APD channel.

Parameter	532-nm APD	1064-nm APD
M, PPM order	256	256
T_s, PPM slot duration	25 ns	25 ns
η, quantum efficiency	0.8	0.38
k, ionization ratio	0.0015	0.02
G, average gain	150 (reported), 387 (measured)	19 (reported), 80 (parameter fit)
I_s, surface leakage current	4.2 nA	100 nA
I_b, bulk leakage current	42 pA	10 pA
T, equivalent noise temperature	1993 K (measured)	6000 K (parameter fit)
R_L, load resistance	10 kΩ	1.5 kΩ
$\bar{n}_{bi}$, mean number incident background photons	0, 100	0
$\bar{n}_{si}$, mean number incident signal photons	∼30–180	∼250–1800

and measuring the noise-power output of the preamplifier. The 532-nm APD gain values were measured in the following manner. From [4], the gain, G, was given by

$$G = \frac{V}{P_{av}} \frac{h\nu}{q\eta Q' g} \tag{5}$$

where V is the average peak voltage of the APD output signal, P_{av} is the average incident optical power in watts, ν is the optical frequency, η is the APD quantum efficiency, Q' is the number of slots between pulses, and g is the transimpedance amplifier gain, which in this case is taken to be the feedback resistance value of 10 kΩ. The results of these measurements under the various APD gain "modes" and laser pulse repetition rates are given in Table 2. Gain and temperature measurements were unable to be taken for the 1064-nm APD, so the values of these two parameters were estimated by fitting the pdf to the experimental histogram. Use of the manufacturer-provided average gain value and room temperature resulted in an unreasonably large discrepancy between analytical and empirical curves.

Table 2. Measured gain values for the 532-nm APD.

Nominal value	Pulse repetition rate, kHz	Measured value
0	10	1.407
	50	1.352
	75	1.326
	100	1.245
150	10	516.87
	50	386.99
	75	362.20
	100	242.216
300	10	1112.5
	50	951.37
	75	865.24
	100	737.96

Using the parameters in Table 1, the pdf's for the Webb+Gaussian model of the APD were computed for each collection run. The density function requires computation of a convolution integral for each point on the curve. A comparison of the empirical and theoretical pdf's is shown in Figs. 2 and 3 for the 532-nm APD when there are 0 and 100 incident background photons, $\bar{n}_{bi}$, per slot, and in Fig. 4 for the 1064-nm APD when there is just 0 incident background photons per slot. In each figure, plots of the lowest signal power (in terms of incident signal photons per slot, $\bar{n}_{si}$) and highest signal power in the data collection run are shown. There was a certain amount of bias that varied with the background power, so in all of the figures the empirical curves were shifted so that the empirical noise pdf peak lined up with the theoretical noise pdf peak. The separation between signal and noise curves and the width of these curves, however, are the features that predict error performance.

As may be seen in Figs. 2 and 3, there are minor quantitative discrepancies between the empirical and theoretical pdf's in the 532-nm data. The empirical noise pdf's are smooth and fairly Gaussian in appearance, while the empirical signal pdf's are more irregular, due to the smaller sample size of the

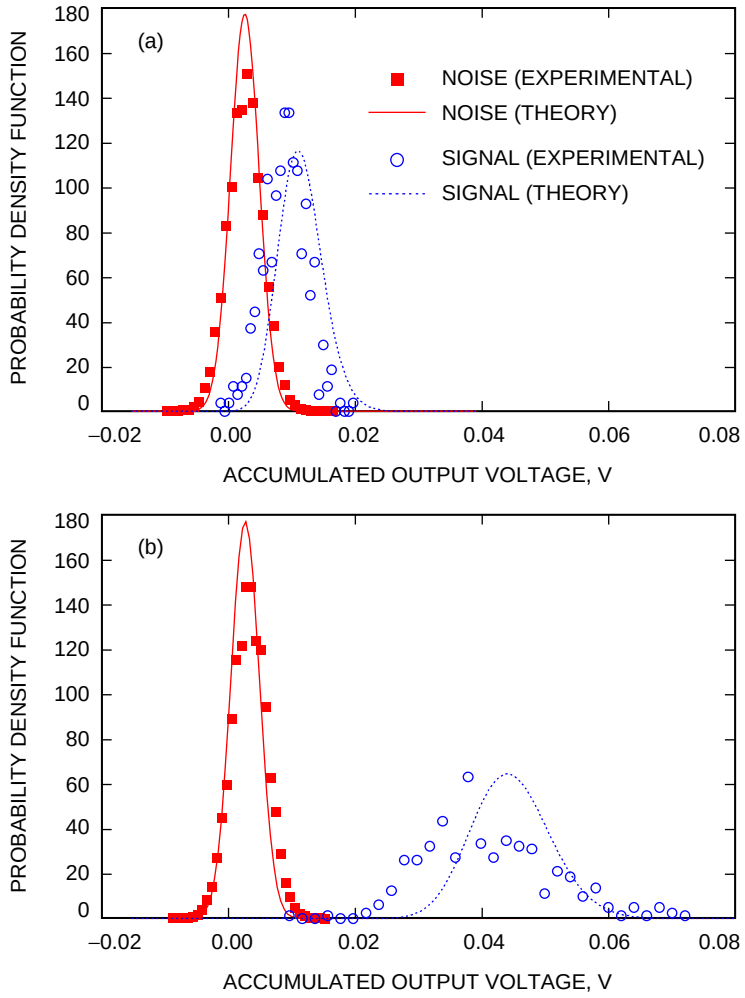

Fig. 2. Comparison of empirical and theoretical pdf's, 532-nm APD, $\bar{n}_{bi} = 0$: (a) $\bar{n}_{si} = 36$ and (b) $\bar{n}_{si} = 170$.

signal slots. As these pdf's are close to Gaussian in shape, they may be characterized by their means and variances, so we shall discuss the discrepancies between the empirical and theoretical results in those terms. In all of the plots shown, the separation between the means of the empirical noise and signal distributions is reasonably close to the separation between the theoretical curves, although this empirical separation is slightly less for the zero-background plots of Fig. 2. In addition, the empirical variances are greater than predicted by theory in Fig. 2, but less than predicted by theory in the plots of Fig. 3. A possible explanation for these discrepancies could be imperfect knowledge of APD parameters that were not measured, such as ionization ratio or leakage currents.

Figure 4 shows the signal and noise distributions for the 1064-nm APD while letting the APD gain and equivalent noise temperature be free parameters chosen to fit the theoretical pdf's to the empirical pdf's (given in Table 1). These parameters were set in this manner due to the lack of measured values for the gain and temperature, which do have a large effect on the properties of the density curves. Even with this parameter fit, we observe noticeable sidelobes in the empirical pdf's shown in Fig. 4. In addition to the same error sources mentioned before, the 1064-nm detector data suffered from some ringing effects in the detected signal pulses as well as an unwanted 350-kHz oscillation due to RF pickup from other sources (such as the power supply on the HVTC board to which the 1064-nm APD is integrated). This could result in the distortion of the noise and signal histograms evident in the figures. In any case, the

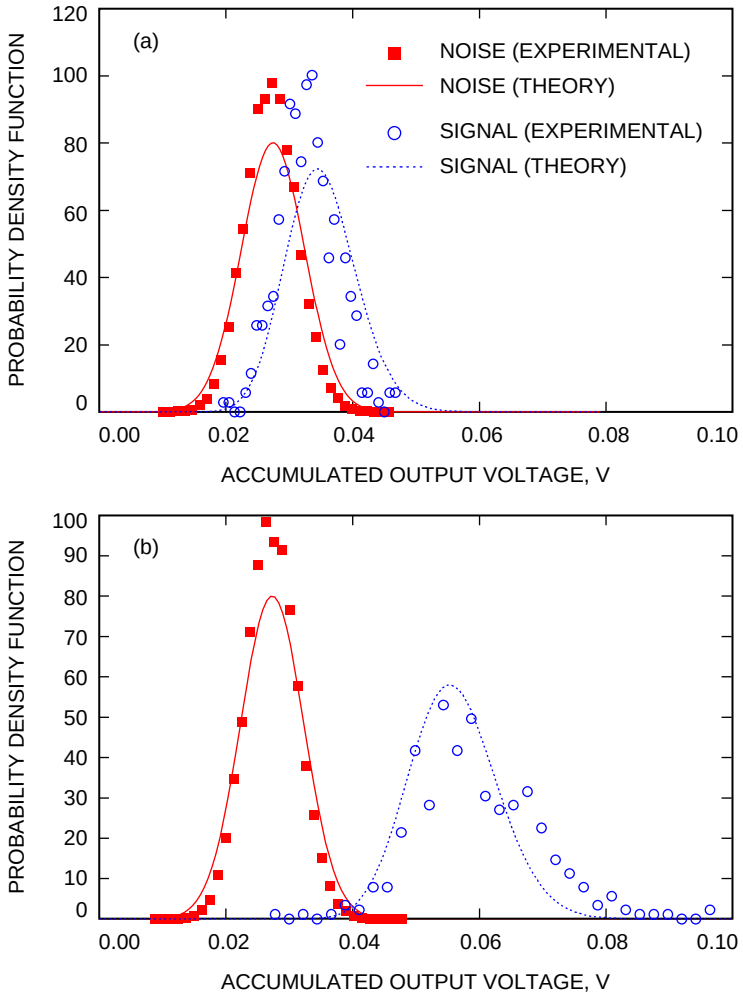

Fig. 3. Comparison of empirical and theoretical pdf's, 532-nm APD, $\bar{n}_{bi} = 100$: (a) $\bar{n}_{si} = 31$ and (b) $\bar{n}_{si} = 116$.

uncertainty in parameter values for this particular detector as well as the poor isolation properties of the board require further investigation in order to make definitive conclusions regarding its performance.

C. Bit-Error Rate Comparisons

The slot counts collected to create the empirical pdf's may also be used to calculate the empirical uncoded symbol-error rate (SER) by comparing each signal slot count with 255 non-signal slot counts. The theoretical uncoded SER is calculated using Eq. (4), with both the Webb+Gaussian as well as the slightly less accurate completely Gaussian approximation used for the APD output density function. The uncoded symbol-error rate is converted to an uncoded bit-error rate (BER) via the expression

$$\mathrm{BER} = \frac{M(\mathrm{SER})}{2(M-1)} \tag{6}$$

where $M = 256$ is the PPM order. A comparison of the empirical and theoretical BERs is shown in Figs. 5 and 6 for the 532-nm and 1064-nm detector data, respectively. Because only 400 symbols were processed for each empirical BER point, we also computed the 95 percent confidence interval based on

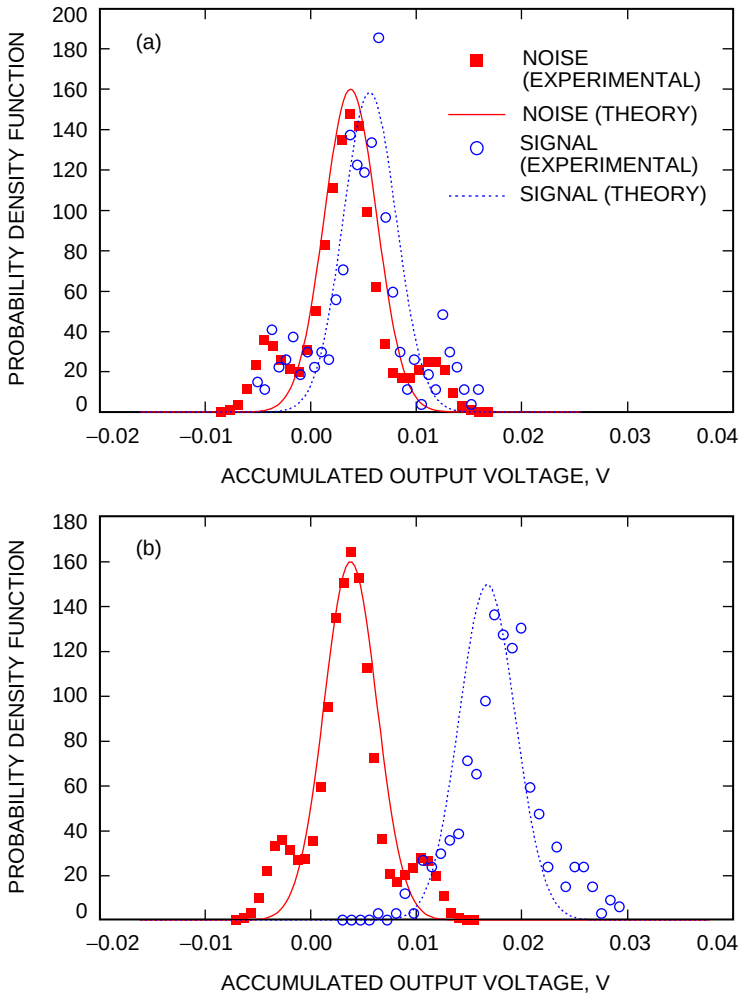

Fig. 4. Comparison of empirical and theoretical pdf's, 1064-nm APD, $\bar{n}_{bi}$ = 0, with G = 80 and T = 6000 K chosen to fit analytical curves to empirical curves: (a) $\bar{n}_{si}$ = 252 and (b) $\bar{n}_{si}$ = 1778.

sampling from a binomial distribution. Note that at lower error probabilities the error bars are quite large due to the lack of an adequate sample size.

The bit-error rates shown in Fig. 5 are not inconsistent with the pdf's shown earlier. In Fig. 2, the empirical separation between the noise and signal pdf's is slightly less than theoretically predicted for the 532-nm APD, and the variance appears greater. In Fig. 3, the variance of the empirical curves appears to be less than that of the theoretical curves. These qualities are reflected in the BERs of Fig. 5, which show an empirical BER that is about 1.5 dB higher than predicted with the Webb+Gaussian analytical model for the $\bar{n}_{bi} = 0$ case, and an empirical BER for the $\bar{n}_{bi} = 100$ case that is about 0.3 dB lower than the Webb+Gaussian model would predict. It is also worth noting the the Gaussian and Webb+Gaussian analytical models diverge for the parameters of Fig. 5, with the simpler Gaussian model over-predicting the BER by about 0.2 dB at a 0.001 BER.

It is more difficult to judge the consistency of the $\bar{n}_{bi} = 0$ 1064-nm APD bit-error rates with the pdf's. In this case, the empirical bit-error rates using the standard "pick maximum slot value" PPM symbol decision rule are larger than theoretically predicted by about 0.7 dB. Note that the theoretical curve

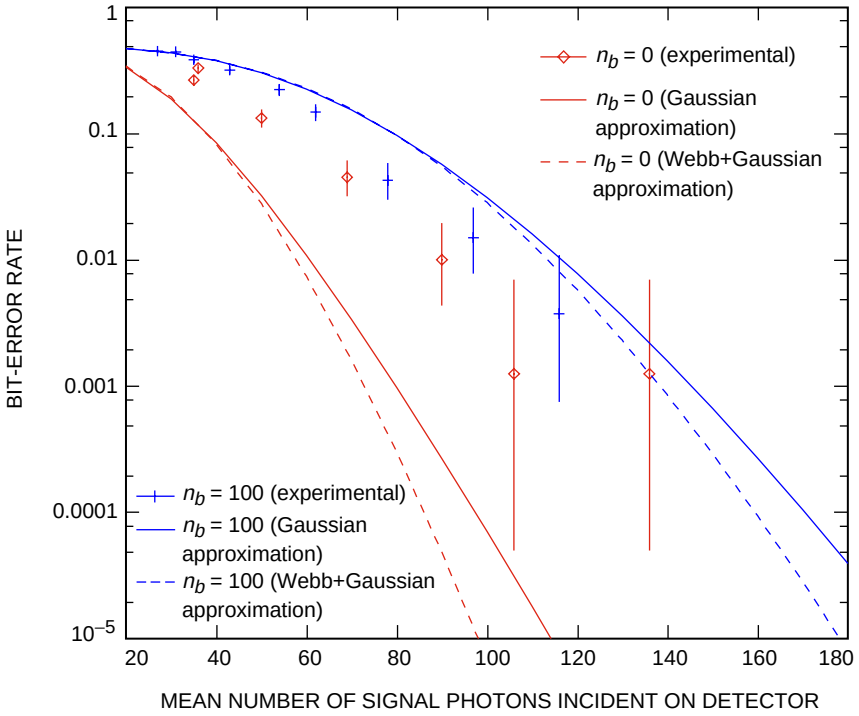

Fig. 5. Comparison of empirical and theoretical bit-error rates, 532-nm APD, $\bar{n}_{bi} = 0$ and $\bar{n}_{bi} = 100$.

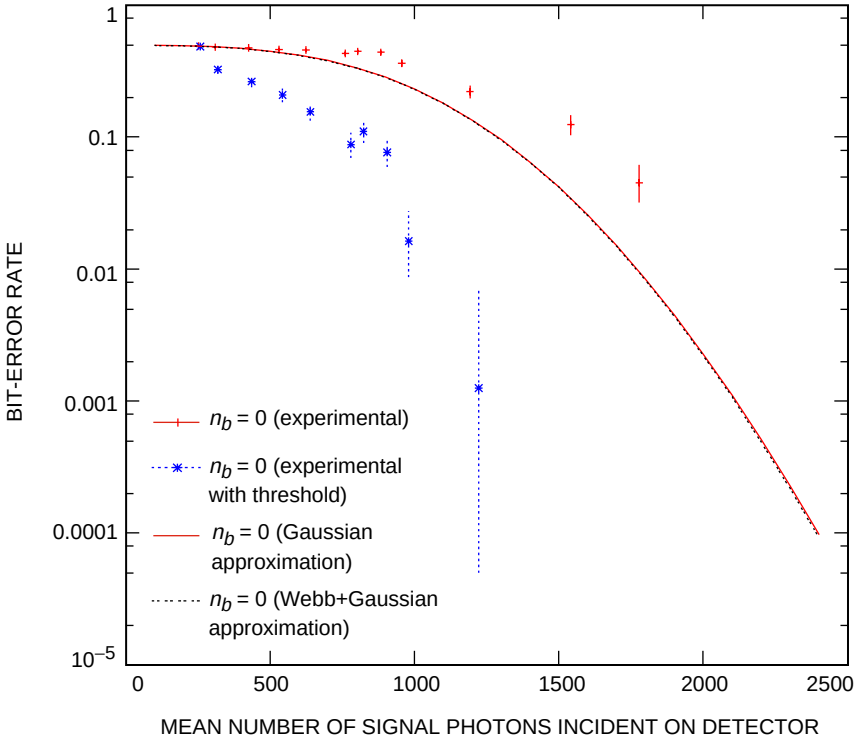

Fig. 6. Comparison of empirical and theoretical bit-error rates, 1064-nm APD, $\bar{n}_{bi} = 0$.

assumes the same gain and temperature values used for the pdf's, i.e., $G = 80$ and $T = 6000$ K, and that although these parameters provided a closer fit of the empirical pdf's to the analytical pdf's, these data are altogether marred by effects such as ringing and RF pickup. We also observe that using an ad hoc threshold to discriminate against the ringing effect prior to choosing the largest slot in the PPM detection process results in a BER that is 2 to 3 dB less than the "maximum likelihood" BER. Note that this result, which on the surface appears incorrect, is due to the fact that the maximum-likelihood rule of [6] assumes ideal signal pulses without the ringing or oscillatory effects displayed by the 1064-nm APD. While it is comforting to know that measures may be taken to improve BER performance under non-ideal conditions, more effort must be put into suppressing these unwanted effects in the first place.

By using the ad hoc PPM decision rule for the 1064-nm APD data, a BER of 0.01 is met with approximately 1000 incident signal photons. On the other hand, the uncoded BER design requirement of 0.01 is met by the 532-nm detector with approximately 90 incident signal photons at zero background levels.

IV. Slot Synchronization

In the previous sections, knowledge of PPM symbol and slot boundaries was provided through use of a laser trigger file that indicated when a PPM laser pulse was fired. Here we show some preliminary results on performance of a slot synchronization loop that provides PPM slot timing. We still assume that the location of PPM symbol boundaries is known.

Slot synchronization is achieved using a delay tracking loop that has been described and analyzed in [10,11] and is shown in Fig. 7. The noisy version of the PPM signal output by the APD is multiplied by a periodic square wave at the slot frequency and integrated over a slot time to generate an error signal that is gated by a threshold detector over the same slot time in order to eliminate noise slots from the loop. This signal is then accumulated over a certain number of symbol frames and converted to an integer number of samples for correcting the slot timing. Although not used here, a loop filter may also be used to accumulate the error signal and track dynamics in the slot timing.

Due to the less desirable features of the 1064-nm APD data mentioned earlier, only the 532-nm APD data were tested here. In implementing the slot synchronization loop for the purposes of this article, the S-curve, or expected value of the error signal as a function of sample offset, was calculated experimentally for each operating point of signal and background level in order to determine the loop gain for normalizing the error signal. An example is shown in Fig. 8. Furthermore, the threshold values for eliminating noise

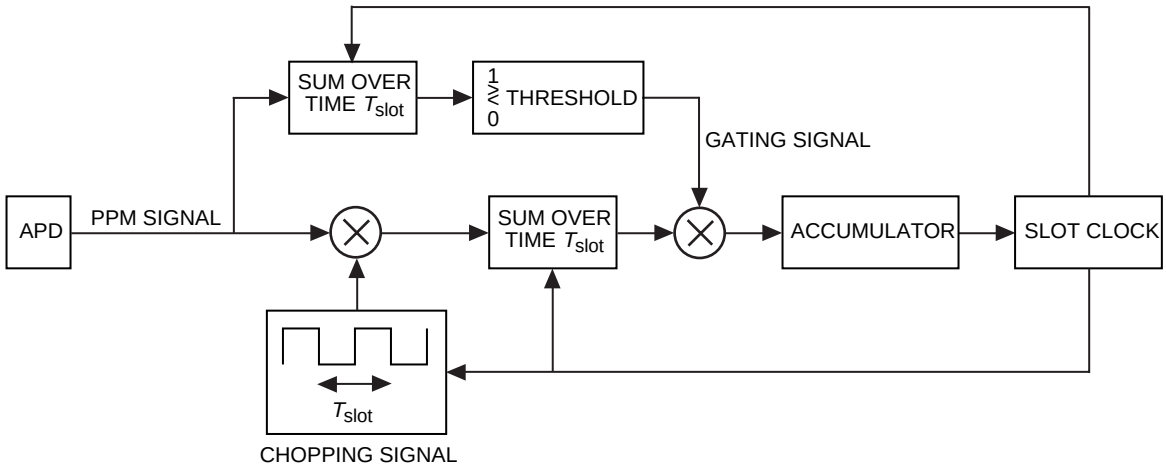

Fig. 7. The PPM slot synchronization loop.

slots are chosen ad hoc by visual inspection of the APD output data stream. A practical implementation of this tracking loop would require the real-time estimation of these quantities.

Because the data sets consisted of a relatively small number of signals (∼400), the data files were looped in order to test this slot synchronization loop. The correlated data that resulted from this are not suitable for calculation of mean-squared tracking error. However, bit-error rates were calculated and are presented here to show the effect of the timing loop on error-rate performance. Figure 9 compares the bit-error rates for the 532-nm APD using slot timing derived from the tracking loop with bit-error rates calculated assuming ideal slot timing knowledge. From this figure we observe that little loss is incurred through use of the tracking loop timing, although longer data sets need to be tested to obtain statistically significant results.

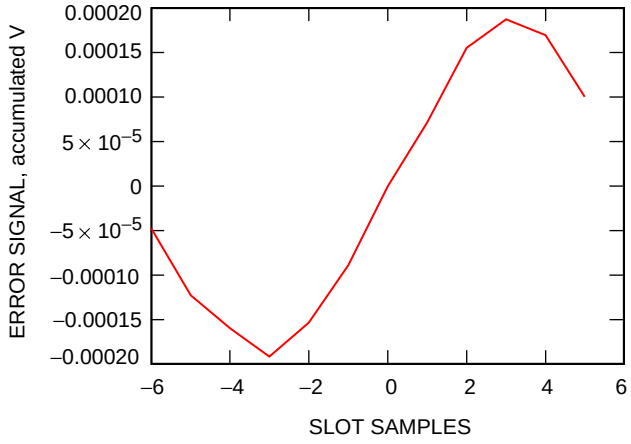

Fig. 8. An experimental slot synchronization S-curve for 532-nm APD data, $\bar{n}_{bi}$ = 0 and $\bar{n}_{si}$ = 170.

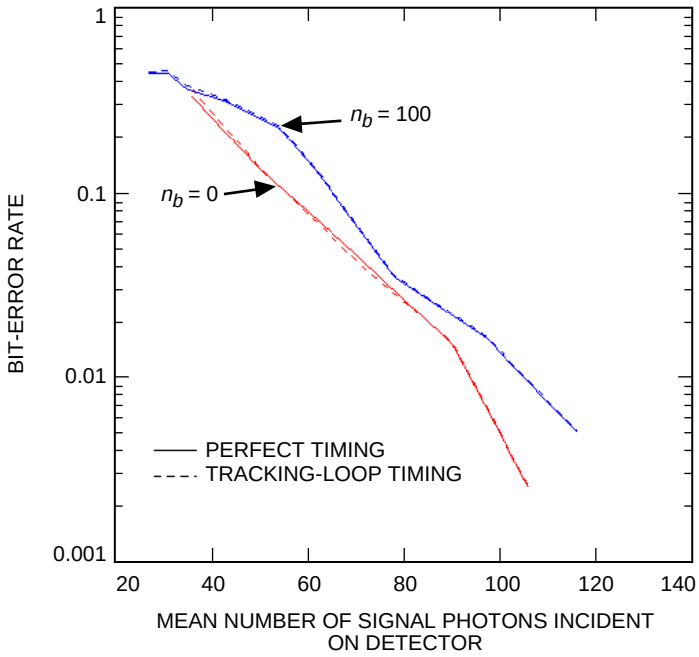

Fig. 9. Bit-error probabilities using a slot synchronization tracking loop, 532-nm APD, $\bar{n}_{bi}$ = 0 and $\bar{n}_{bi}$ = 100.

V. Conclusions

In this article, the results of ongoing experiments using commercially available silicon avalanche photodiodes for pulse-position modulation detection and slot synchronization were compared with theoretical models in order to characterize the real-world performance of these detectors. Both a 532-nm and a 1064-nm APD were tested through the construction of empirical probability density functions for signal and noise PPM slots and through the calculation of bit-error probabilities. There is reasonable agreement between the experimental results and theory for the 532-nm APD, but significant discrepancies exist between experimental and theoretical results for the 1064-nm APD unless the noise equivalent temperature is assumed to be very high and the average APD gain is assumed to be higher than reported. Deintegrating the 1064-nm APD from the HVTC board will allow for more stringent controls on parameter measurements and the decoupling of interference sources. Specifically, an external power supply may then be used, removing one source of RF pickup. Continuing work will focus upon refinement of parameter measurement techniques. In addition, more accurate modeling of the laser output signal power may be investigated in order to improve correspondence between theory and experiment.

While matching the experimental data with theoretical models is necessary, we can arrive at another conclusion just on the basis of the comparison between the laboratory performance of the two different wavelength detectors. Although the 1064-nm wavelength is superior to the 532-nm wavelength in terms of transmission power and atmospheric attenuation, and the 1064-nm detector has better bandwidth properties than the 532-nm APD, the experimental results show that the 1064-nm detector is nonetheless outperformed by the 532-nm APD in terms of bit-error rates. The 1064-nm detector sensitivity in terms of required signal photons per pulse is a factor of 10 worse than that of the 532-nm detector. RF pickup, lower quantum efficiency, and poorer gain and excess noise characteristics are all contributing factors to this. Certainly in order to take advantage of the system advantages at 1064 nm, the detector performance must be improved.

Finally, it was shown that a simple delay tracking loop may be used effectively for slot synchronization on the 532-nm APD data with little resulting loss in bit-error probability. Larger data sets must be used to quantify synchronization performance more precisely.

References

[1] T.-Y. Yan and C.-C. Chen, "Design and Development of a Baseline Deep Space Optical PPM Transceiver," *Proceedings of SPIE, Free-Space Laser Communications Technologies XI*, G. S. Mecherle, ed., vol. 3615, pp. 154–169, 1999.

[2] C.-C. Chen, "Figure of Merit for Direct-Detection Optical Channels," *The Telecommunications and Data Acquisition Progress Report 42-109, January–March 1992*, Jet Propulsion Laboratory, Pasadena, California, pp. 136–151, May 15, 1992.
http://tmo.jpl.nasa.gov/tmo/progress_report/42-109/109L.PDF

[3] G. G. Ortiz, J. V. Sandusky, and A. Biswas, "Design of an Opto-Electronic Receiver for Deep-Space Optical Communications," *The Telecommunications and Mission Operations Progress Report 42-142, April–June 2000*, Jet Propulsion Laboratory, Pasadena, California, pp. 1–17, August 15, 2000.
http://tmo.jpl.nasa.gov/tmo/progress_report/42-142/142I.pdf

[4] F. M. Davidson and X. Sun, "Gaussian Approximation Versus Nearly Exact Performance Analysis of Optical Communications Systems with PPM Signaling and APD Receivers," *IEEE Transactions on Communications*, vol. COM-36, pp. 1185–1192, November 1988.

[5] G. L. Unger, M. A. Krainak, and X. Sun, "Comparison of Direct 50 Mbps Q-PPM Receiver Performance for AlGaAs and Nd Doped Laser Transmitters," *Proceedings of SPIE Free-Space Laser Communications Technologies IV*, vol. 1635, no. 2, pp. 2–9, 1992.

[6] V. Vilnrotter, M. Simon, and M. Srinivasan, "Maximum Likelihood Detection of PPM Signals Governed by an Arbitrary Point Process Plus Additive Gaussian Noise," *Electronics Letters*, vol. 35, pp. 1132–1133, July 1999.

[7] H. Plaessmann, K. S. Yamada, C. E. Rich, and W. M. Grossman, "Sub-Nanosecond Pulse Generation from Diode Pumped Acousto-Optically Q-Switched Solid-State Lasers," *Applied Optics*, vol. 32, pp. 6616–6619, 1993.

[8] R. J. McIntyre, "The Distribution of Gains in Uniformly Multiplying Avalanche Photodiodes: Theory," *IEEE Transactions on Electron Devices*, vol. ED-19, pp. 703–713, June 1972.

[9] P. P. Webb, R. J. McIntyre, and J. Conradi, "Properties of Avalanche Photodiodes," *RCA Review*, vol. 35, pp. 234–278, June 1974.

[10] V. A. Vilnrotter, E. R. Rodemich, and H. H. Tan, "A Synchronization Technique for Optical PPM Signals," *The Telecommunications and Data Acquisition Progress Report 42-87, July–September 1986*, Jet Propulsion Laboratory, Pasadena, California, pp. 24–31, November 15, 1986.
http://tmo.jpl.nasa.gov/tmo/progress_report/42-87/87C.PDF

[11] R. M. Gagliardi and S. Karp, *Optical Communications*, New York: John Wiley and Sons, Inc., 1995.